# Automated Multiscale Morphometry of Muscle Disease From Second Harmonic Generation Microscopy Using Tensor-Based Image Processing

Christoph S. Garbe*, *Member, IEEE*, Andreas Buttgereit, Sebastian Schürmann, and Oliver Friedrich

***Abstract*—Practically, all chronic diseases are characterized by tissue remodeling that alters organ and cellular function through changes to normal organ architecture. Some morphometric alterations become irreversible and account for disease progression even on cellular levels. Early diagnostics to categorize tissue alterations, as well as monitoring progression or remission of disturbed cytoarchitecture upon treatment in the same individual, are a new emerging field. They strongly challenge spatial resolution and require advanced imaging techniques and strategies for detecting morphological changes. We use a combined second harmonic generation (SHG) microscopy and automated image processing approach to quantify morphology in an animal model of inherited Duchenne muscular dystrophy (*mdx* mouse) with age. Multiphoton XYZ image stacks from tissue slices reveal vast morphological deviation in muscles from old *mdx* mice at different scales of cytoskeleton architecture: cell calibers are irregular, myofibrils within cells are twisted, and sarcomere lattice disruptions (detected as "verniers") are larger in number compared to samples from healthy mice. In young *mdx* mice, such alterations are only minor. The boundary-tensor approach, adapted and optimized for SHG data, is a suitable approach to allow quick quantitative morphometry in whole tissue slices. The overall detection performance of the automated algorithm compares very well with manual "*by eye*" detection, the latter being time consuming and prone to subjective errors. Our algorithm outperfoms manual detection by time with similar reliability. This approach will be an important prerequisite for the implementation of a clinical image databases to diagnose and monitor specific morphological alterations in chronic (muscle) diseases.**

***Index Terms*—Automated detection, muscle architecture, second harmonic generation (SHG) microscopy, structure analysis.**

Manuscript received April 11, 2011; revised April 11, 2011; accepted August 15, 2011. Date of publication September 8, 2011; date of current version December 21, 2011. This work was supported by the German Research Foundation (DFG) in part (Garbe) through the "Heidelberg Graduate School of Mathematical and Computational Methods for the Sciences" (DFG GSC 220) and (Friedrich) through the "Erlangen Graduate School in Advanced Optical Technologies", both within the German Excellence Initiative. *Asterisk indicates corresponding author.*

*C. S. Garbe is with the Interdisciplinary Center for Scientific Computing, University of Heidelberg, 69115 Heidelberg, Germany (e-mail: Christoph.Garbe@uni-heidelberg.de).

A. Buttgereit, S. Schürmann, and O. Friedrich were with the University of Heidelberg, 69115 Heidelberg, Germany. They are now with the Institute of Medical Biotechnology, Friedrich-Alexander-University Erlangen-Nuremberg, 91054 Erlangen, Germany (e-mail: Andreas.Buttgereit@urz.uni-heidelberg.de; Sebastian.Schuermann@mbt.uni-erlangen.de; Oliver.Friedrich@mbt.uni-erlangen.de).

Color versions of one or more of the figures in this paper are available online at http://ieeexplore.ieee.org.

Digital Object Identifier 10.1109/TBME.2011.2167325

## I. Introduction

IMAGING techniques in combination with image-processing strategies have become indispensable in biomedical research to elucidate biomolecule structures and function [1], [2], or in medical diagnostics to track disease states, progression, or remission [3], [4]. Common far-field imaging techniques, e.g., magnetic resonance imaging, computed tomography, or ultrasound, have the advantage of being noninvasive, yet suffer from restricted spatial resolution. Recently, emerging efforts to combine photonic or photoacoustic imaging and endoscopy have enabled close inspection of tissues for enhanced resolution of structure and function (see, e.g., [5]). Particularly, novel laser-based multiphoton techniques are currently being developed to monitor disease states [6], [7]. Such approaches will initiate a new era of cell-based imaging in patients. Apart from cellular resolution, specificity of the signal is also crucial with regard to tissue imaging. Second harmonic generation (SHG) microscopy takes advantage of a nonlinear and coherent frequency-doubling optical effect that is inherent to very few biomolecules, i.e., collagen I and myosin II and allows label-free imaging of living cells [8]. Especially for muscle, SHG microscopy allows detailed reconstruction of subcellular cyto-architecture in normal and disease states [9], [10]. In skeletal muscle, the regular arrangement of the motor-protein myosin II within sarcomeres allows perfect label-free imaging of single cells *in situ*. Hundreds of sarcomeres in series make up a myofibril and a muscle cell consists of many parallel myofibrils (see Fig. 1). Therefore, muscle ultrastructure can be represented by different morphometry scales that project from cellular down to myofibrillar and sarcomere level. This becomes very important when comparing healthy tissue with muscle disorders. Most muscle diseases, either acquired or inherited, cohere with a chronic course that gives rise to tissue inflammation and remodeling [10], [11]. One well-studied example is Duchenne muscular dystrophy (DMD) that affects individuals through complete absence of the mechanically stabilizing protein dystrophin [12]. During the fatal course of the disease, muscle tissue constantly becomes replaced by fibrotic tissue. On the cellular level, progression of the disease is reflected by vast morphological alterations, i.e., cellular fiber branching or out-of-register twists of myofibrils [10], [13]. The *mdx* mouse is an animal model that reflects some of the human pathologies regarding tissue remodeling. SHG microscopy was recently applied to quantify micromorphology in muscle cells from this model [10]. However, the morphometric scales for cells embedded in the tissue architecture are still missing to date. This is an important issue for the successful

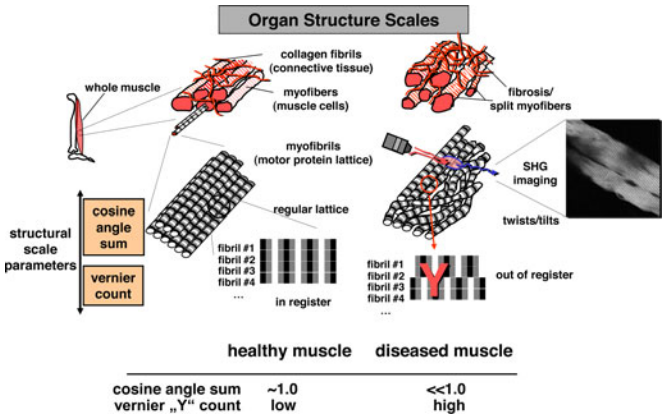


Fig. 1. Muscle architecture comprises of parallely arranged myofibers (i.e., muscle cells) linked via connective tissue on multiple scales. Each single cell contains a matrix of parallel myofibrils that consist of elementary contractile units, the sarcomeres. The structure is highly ordered in healthy tissue but architecture becomes disturbed on all levels during chronic diseases involving tissue remodeling. Architectural deviations can be represented by different parameters at each scale.

implementation of miniaturized SHG imaging in flexible endoscopes for "*in vivo*" disease morphometry in a clinical setting. Such advances have to be closely linked to establishing database knowledge of how muscle tissue in the disease state is represented in the context of whole muscle sections. To this end, we present first detailed recordings of SHG signals from muscle slices of normal (wild-type, wt) and dystrophic *mdx* mice at different ages to emphasize the progression of ultrastructural deviation with age. For quantitative morphometric analysis of the 3-D aspect of tissue slices, we apply image processing algorithms based on the boundary tensor [14] (see Section III-A).

From the image processing routines, we extract sensitive morphometric parameters that are inherent to different scales of muscle morphology, i.e., by the cosine angle sum and vernier counts. "Verniers" refer to a local disruption of the regular sarcomere lattice giving rise to "Y"-like local structured patterns that are being detected after image segmentation. The cosine angle sum $\overline{\cos}$ is defined as

$$\overline{\cos} = \frac{1}{|\Omega|} \sum_{(x,y)\in\Omega} \cos\left(\phi(x,y)\right) \tag{1}$$

where $\Omega$ denotes the domain of the imaged "foreground" sacromere lattice, $|\Omega|$ is the number of pixels of the sacomere lattice visualized in an image, and $\phi(x,y)$ is the local direction $\phi'(x,y)$ of the structures subtracted from the dominant direction of all the structures in the image $\mathrm{mean}(\phi'(x,y))$, or $\phi(x,y) = \phi'(x,y) - \mathrm{mean}(\phi'(x,y))$. For a completely isotropic structure, $\overline{cos} = 0$, while $\overline{cos} = 1$ for linear patterns. We propose that this technology will be suitable to establish an exhaustive morphometric image database providing diagnostic biomarkers for different kinds of myopathies that will be useful for future clinical implementation.

## II. Experimental Procedures

For multiphoton SHG microscopy of whole tissue slices, *M. tibialis cranialis* muscles were dissected from the hindlimb of aged wt (20–24 months) and young and aged dystrophic *mdx* mice (2–3 and 14 months) after killing animals with an overdose of $CO_2$ (all procedures approved by the local Animal Ethics Committee). Muscles were incubated in ice-cold physiological saline containing 1% glutaraldehyde and frozen at $-20\,^{\circ}$C. Tissue slices were cut on a microtome (OTF, Bright Co., U.K.), embedded in a drop of Tissue-Tek compound (Sakura Finetek, The Netherlands) and frozen at $-20^{\circ}$C. Subsequently, thin slices were cut and sandwiched between two coverslips. Single fibers within the tissue layer as well as connective tissue were imaged using our multiphoton microscope in a configuration to collect SHG signals in a forward scattered direction using a nondescanned photomultiplier [15]. Image stacks (XYZ) were obtained using a motorized $z$-stage driven at 0.3-$\mu$m step size. Different magnifications were used to focus on myofibrillar geometry and larger magnifications to detect and label irregularities in the sarcomere lattice ("verniers"). Image processing was performed offline in the MATLAB environment.

## III. Multiscale Image Analysis

The automatic image analysis proposed here is based on a tensorial approach inspired by the boundary tensor as introduced in [14]. We construct a tensor of polar separable filters, optimizing the radial part to the periodic pattern of the tissue. Due to their efficient computation, we employ polar harmonic filters. This analysis is performed in a multiscale framework. The energy and direction of the myofilaments represented as cylindrical tubes in the images are computed. Based on the scale of the observed signal, cosine angles of the directional signal are used to quantify structural coherency of neighboring filaments. On smaller scales, the ridges of the gradient field of the signal direction are identified with locations of local disruption of the regular striation pattern, resulting in "verniers." These can be segmented by global thresholding.

### A. Tensor Representation

The $N$-dimensional Riesz transform is defined in the Fourier domain as $\mathcal{H}_N[H(\vec{u})] = i\frac{\vec{u}}{|\vec{u}|}H(\vec{u})$ [16] and in the spatial domain, respectively, as

$$\mathcal{H}_N[h(\vec{x})] = i\frac{\Gamma((N+1)/2)}{\pi^{(N+1)/2}}\left(\frac{-\vec{x}}{|\vec{x}|^{N+1}} \star h(\vec{x})\right). \tag{2}$$

Here, $\Gamma$ is the gamma function, $\vec{u}$ is the $N$-dimensional frequency vector, and $\vec{x}$ the equivalent spatial vector. The convolution is denoted by $\star$. The Riesz transform represents the vector valued Hilbert transform [16]. As is evident from (2), applying the Riesz transform directly to images leads to a bad localization in the spatial domain, as its kernel decreases as $|\vec{x}|^{-N-1}$. Hence, it is combined with a radially symmetric bandpass $K(|\vec{u}|)$. This bandpass is kept constant for all orders of the Riesz transform.

This leads to

$$\vec{b} : \mathcal{H}_N[K(|\vec{u}|)F(\vec{u})] = i\frac{\vec{u}}{|\vec{u}|}K(|\vec{u}|)F(\vec{u}) \tag{3}$$

for the first-order Riesz transform and, respectively, for the second-order transform

$$\mathbf{A} : \mathcal{H}_N^2[K(|\vec{u}|)F(\vec{u})] = -\frac{\vec{u}\vec{u}^\top}{|\vec{u}|^2}K(|\vec{u}|)F(\vec{u}) \tag{4}$$

where $\top$ denotes the transpose. Following [17], the boundary tensor $\mathbf{B}$ is defined as $\mathbf{B} = \vec{b}\vec{b}^\top + \mathbf{A}\mathbf{A}^\top$.

For an efficient computation, the bandpass $K$ is generally implemented as a Laplacian of Gaussian

$$K(|\vec{u}|, \sigma) = |u|^2 e^{-\frac{|\vec{u}|^2}{2\sigma^2}}. \tag{5}$$

We fine tune the bandpass to the pattern of the imaged tissue. With the frequency of the pattern $f$, this leads to

$$K_f(|\vec{u}|, \sigma) = -e^{-\frac{(|\vec{u}|-f)^2}{2\sigma^2}}. \tag{6}$$

With the phase $\varphi$ of the signal, the resulting filter polar harmonic separable filters are thus

$$b_1 = i \cdot \cos(\varphi)K_f(|\vec{u}|, \sigma),\ b_2 = i \cdot \sin(\varphi)K_f(|\vec{u}|, \sigma)$$
$$A_{11} = -\cos(\varphi)^2 K_f(|\vec{u}|, \sigma)$$
$$A_{12} = A_{21} = -\sin(\varphi)\cos(\varphi)K_f(|\vec{u}|, \sigma)$$
$$A_{22} = -\sin(\varphi)^2 K_f(|\vec{u}|, \sigma).$$

We construct the tensor $\mathbf{B} = \mathbf{E} + \mathbf{O}$ from its even $\mathbf{E}$ and odd $\mathbf{O}$ components given by

$$O_{kl} = b_k \cdot b_l \tag{7}$$
$$E_{11} = A_{11}^2 + A_{12}^2 \text{ and } E_{22} = A_{22}^2 + A_{12}^2 \tag{8}$$
$$E_{11} = A_{11} \cdot A_{12} + A_{12} \cdot A_{22}. \tag{9}$$

Several important features can be extracted from the tensor $\mathbf{B}$. With respect to this application, such features are the energy $E$ and the direction $\phi$ of the signal, and are given by

$$E = B_{11} + B_{22} \text{ and } \phi = \frac{1}{2}\arctan\left(\frac{2B_{12}}{B_{11} - B_{22}}\right). \tag{10}$$

### B. Image Processing

A scale space is constructed from the 3-D image stacks through a Gaussian pyramid. On each level, the dominant frequency $f$ of the signal is extracted through a Wavelet analysis. Based on $f$, both the energy $E$ and the direction $\phi$ are extracted as detailed in Section III-A. Segmentation of the filaments from the background is performed by thresholding $E$. Multiple filaments are detected by performing a simple labeling of the connected components of the segmented images. For each of these filaments, the average of the cosine angle for each pixel $\overline{\cos}$ is computed from $\phi$ following (1). This is a direct measure for the coherency and structural integrity of the filaments.

On a smaller scale, the number and location of verniers is sought. *Y*-structures can be thought of as a local change in the direction of the signal. Hence, they are located by performing a ridge detection in $\phi$. This is performed by analyzing the eigenvalues $\lambda_i$ of the Hessian matrix of $\phi$. Thresholding the measure $m = \frac{\lambda_1 - \lambda_2}{\lambda_1 + \lambda_2} \in [0, 1]$ is performed for segmenting areas of verniers. For a count of the number of verniers, these segmented areas are multiplied by a threshold segmentation of the phase $\varphi$ of the signal. Labeling of the connected components of these segmented areas results in a count of the number of verniers. This procedure is shown in Fig. 2.

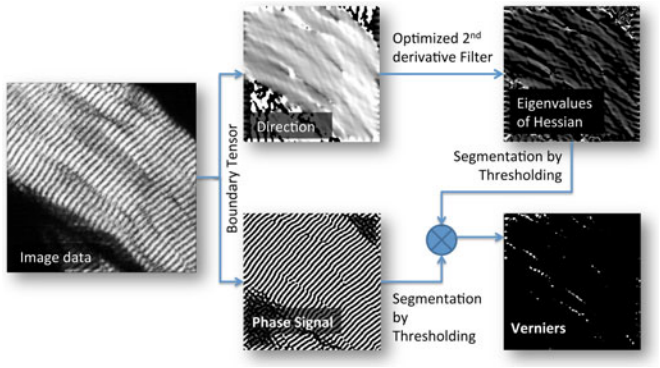


Fig. 2. Outline of the algorithmic framework. The boundary tensor $\mathbf{B}$ is constructed from the image data. Both, direction $\phi$ and phase $\varphi$ of the signal are extracted from $\mathbf{B}$. The largest eigenvalue of the Hessian of $\phi$ is thresholded. Multiplying this image with the segmented phase $\varphi$ yields the verniers, which are counted by labeling connected components.

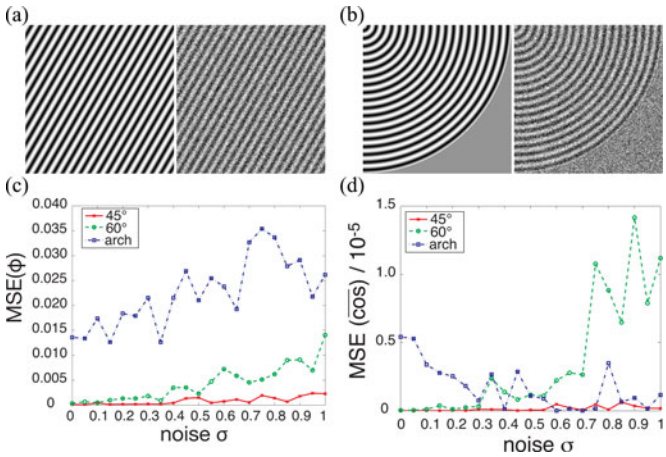


Fig. 3. Accuracy analysis of direction estimation and of $\overline{\cos}$. (a) Synthetic test patterns with $\alpha_2 = 60°$ and the ground truth $\overline{\cos}_{\mathrm{GT}} = 1$. (b) Arch for which $\overline{\cos}_{\mathrm{GT}} = 0.9$ (resolution and frequency $f' = f/4$ have been changed for display purposes). The patterns are shown without noise ($\sigma = 0$) and with medium noise ($\sigma = 0.5$). MSE of (c) $\phi$ and (d) $\overline{\cos}$ is shown for noise levels ranging from $\sigma = [0, 1]$ gray values.

The entire analysis can be performed in full 3-D, or on the 2-D slices individually. To reduce computational complexity, we conduct our computation on each 2-D slice separately. An additional stabilization of the results can be achieved by requiring that retrieved verniers to be present in two neighboring slices.

The image-based analysis is highly robust to noise. The bandpass $\sigma$ was set to $\sigma = 6$ pixel$^{-1}$ for all data presented here. The dominant frequency $f$ depends on the magnification used but was always in the range $f = [60, 120]$ pixel$^{-1}$. We apply a global threshold to the energy $E$ of the signal to segment the areas of

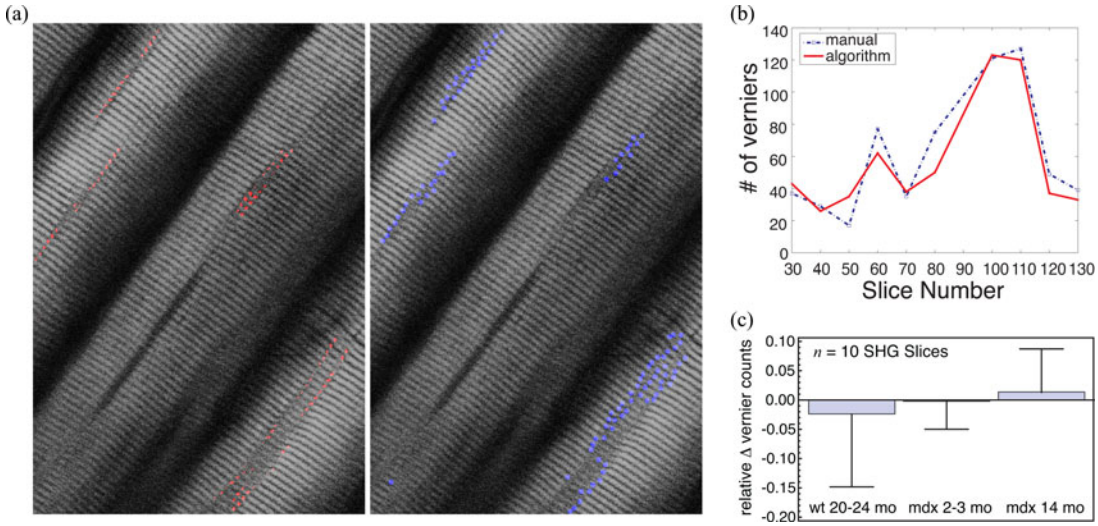


Fig. 4. (a) Segmented verniers by proposed algorithm (red) and manually by expert (blue) on "wt, 20–24 months." (b) Comparison of manual versus automatic for a selection of slices within the "wt, 20–24 months" muscle image stack. (c) Average relative difference $\Delta$verniers = (verniers$_{\mathrm{manual}}$ − verniers$_{\mathrm{algorithm}}$)/verniers$_{\mathrm{manual}}$ and SEM from $n = 10$ slices.

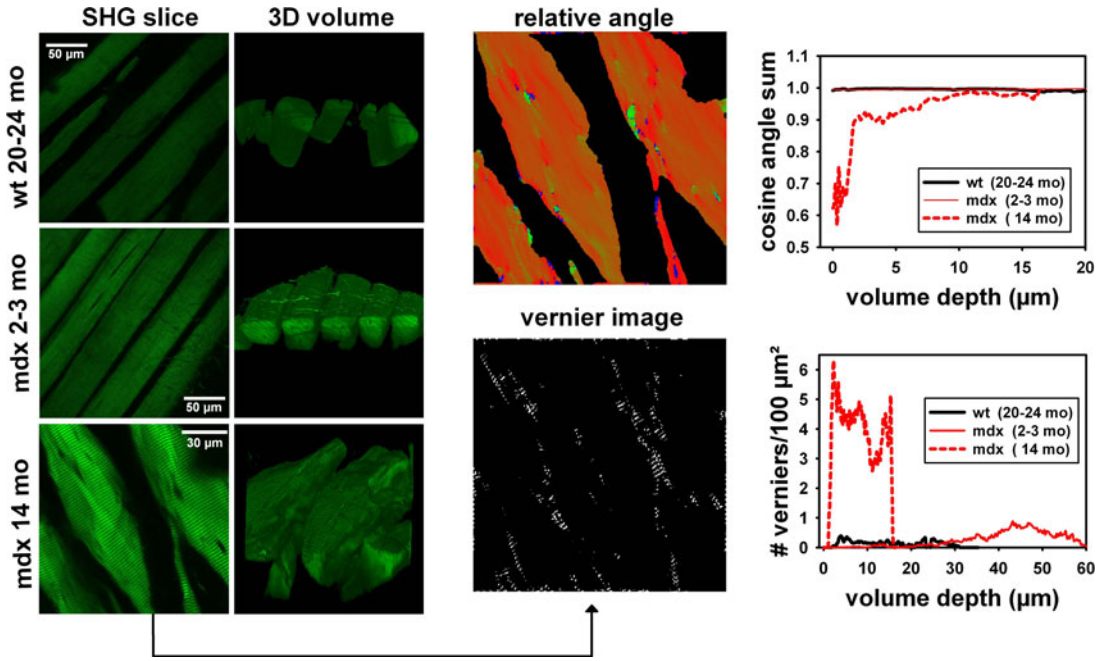


Fig. 5. Typical XY images from within the middle of an XYZ SHG image stack recorded in muscle tissue blocks from an old wt, a young, and an older *mdx* mouse. 3-D rendered volumes are shown also. For the 14-month-old *mdx* mouse, the result from the automated image processing routine showing the detected verniers and the local relative angle deviation from the main fiber trunk on a pseudocolor scale. Within the cell volume, cosine angle sums $\overline{\cos}$ are much reduced and vernier counts markedly increased in the older *mdx* muscle. They are normal, i.e., similar to the wt, in the young *mdx* muscle despite the large age difference between the young *mdx* and the old wt mouse.

interest from the background. Best results were obtained by setting this threshold to 700 for all data.

### C. Data Verification

To verify the accuracy of the proposed algorithm for determining $\overline{\cos}$, we validate it on synthetic test patterns with precisely known cosine angle sums (cf., Fig. 3). We choose this approach as there is no direct means for generating ground truth of this quantity from experimental data in skeletal muscles. We use three test patterns exhibiting a sine pattern inclined at $\alpha_1 = 45°$ and $\alpha_2 = 60°$ with the *Y*-axis, given by $I(x, y) = \sin\{f * (\cos\alpha * x + \sin\alpha * y)\} + 1$ with $f = 0.4709$. This frequency of the signal is similar to the one found in the real tissue data. The third pattern is the same pattern in polar coordinates in one quadrant. We added 21 noise levels $\sigma_i$, ranging from $\sigma_0 = 0$ to $\sigma_{21} = 1$. $\phi$ and $\overline{\cos}$ are computed on these patterns and their mean square error (MSE) is plotted against the noise $\sigma$ (see Fig. 3). MSE is given by $\mathrm{MSE}(\phi) = 1/|\Omega| \sum_{\Omega} (\phi(x, y) - \phi_{GT}(x, y))^2$ and

$\mathrm{MSE}(\overline{\cos}) = (\overline{\cos} - \overline{\cos}_{GT})^2$. We find $\mathrm{MSE}(\overline{\cos})$ to be well below $10^{-5}$ and $\mathrm{MSE}(\phi)$ below $0.035$. The main source of errors are artifacts from the Fourier transform of the nonperiodic patterns.

Besides testing the accuracy of our approach with respect to $\phi$ and $\overline{\cos}$, we also verify the accuracy of the vernier counts. This is done by applying our algorithm to a selection of ten equally distant slices within the image stacks of muscle tissue from *mdx* 2–3 months, *mdx* 14 months, as well as the wild type (20–24 months). The measured counts are then compared to manual vernier counts performed by eye by one of the authors who did not run the automated count detection. Fig. 4(a) shows the overlay of manual and automated counts from one such slice in the wt muscle. The agreement is very good, as the discrepancy of the counts are within the range of scatter for the human subject. This scatter is due to uncertainty in detecting the verniers, which can often be ambiguous and exhaustive for the human subject. However, while our algorithm computes the results of one slice in a couple of seconds, the human counting takes up to 1 h per slide and is prone to visual exhaustion and errors. Fig. 4(c) compares the overall global performance of the automated detection over the manual one, represented as the mean relative count deviations from ten slices within each of the stacks compared. On average, the mean performance deviation is close to zero and compatible with the null hypothesis. The performance difference of the algorithm is thus similar to that of the expert's eye detection.

## IV. Results and Discussion

Fig. 5 shows selected *XY* images from the middle of *XYZ* SHG stacks recorded from thin slices of intact *M. tibialis cranialis* of an old ($\sim 2$ year) wt mouse, a young (2–3 months), and an older (14 months) *mdx* mouse. An example for the volume rendered *XYZ* stack views taken from an arbitrary angle is also shown to demonstrate the relative geometry of single myofibers within the tissue architecture. In young *mdx* muscles, the gross geometry on the intercellular scale is very regular and appeared normal. In the old wt mouse, cells are also largely arranged in parallel, a finding that vastly contrasts the situation in the old *mdx* mouse where cells are branched and interdigitating. From image processing, the relative angle deviation from the main cell orientation (representing the scale of myofibrillar architecture) and the vernier image (representing the scale of sarcomere architecture) are obtained as shown for the older *mdx* fiber (see Fig. 5). The in-depth comparison of cosine angle sums and vernier counts through the tissue slices in the three example preparations confirms our recent findings in single muscle cells enzymatically isolated from the tissue, e.g., $\sim 5$ verniers/100 $\mu$m$^2$ for *mdx* muscle (see Fig. 5, 14 months, and [10, Fig. 3], 12 months). The volume-integrated vernier count in this study is wt: 4.96/1000 $\mu$m$^3$, *mdx*, 2–3 months: 9.77/1000 $\mu$m$^3$, and *mdx*, 14 months: 141.19/1000 $\mu$m$^3$. These findings are important as the confidence for the SHG imaging and ultramorphology image processing technique now extends to the level of whole tissue slices. In young *mdx* muscle of 2–3 months of age, the necrotic phase is predominant; however, massive regeneration with the appearance of fiber branching and morphological alterations appear at some later stage and continue throughout the course of the disease [18].

## V. Conclusion

A multiscale analysis is presented to automatically quantify the morphometry of muscle disease from SHG microscopy. The ongoing chronic inflammation and tissue remodeling is very well represented by the specificity of the SHG signal that maps the ultrastructural geometry within the muscle. Our approach using tissue slices also demonstrates the feasibility of imaging within tissue and the reliable quantification of ultramorphology and cytoarchitecture to map various tissue scales ranging from the multicellular bundle down to the subcellular sarcomere arrangement. A potential next step would be to implement the imaging techniques into microendoscopes for *in vivo* tissue imaging [7]. Based on our automated image processing tools, we plan to provide an image-based platform to collect data and structural information from various disease models and patient samples to be stored in a concise database. This may be implemented as a novel diagnostics aid tool. Additionally, such a database will be central to monitor disease progression or therapeutic efficiency in human muscle diseases.

## Acknowledgment

The authors would like to thank U. Köthe and B. Andres (HCI, University of Heidelberg) for helpful discussions.

## References

[1] T.-W. Nee, S.-M. F. Nee, D.-M. Yang, and Y.-S. Huang, "Scattering polarization by anisotropic biomolecules," *J. Opt. Soc. Am. A. Opt. Image Sci. Vis.*, vol. 25, no. 5, pp. 1030–1038, May 2008.

[2] J. Zhang, R. E. Campbell, A. Y. Ting, and R. Y. Tsien, "Creating new fluorescent probes for cell biology," *Nat. Rev. Mol. Cell Biol.*, vol. 3, no. 12, pp. 906–918, 2002.

[3] H. Handels and J. Ehrhardt, "Medical image computing for computer-supported diagnostics and therapy: Advances and perspectives," *Methods Inf. Med.*, vol. 48, no. 1, pp. 11–17, 2009.

[4] C. Winter, S. Rupp, M. Elter, C. Münzenmayer, H. Gerhäuser, and T. Wittenberg, "Automatic adaptive enhancement for images obtained with fiberscopic endoscopes," *IEEE Trans. Biomed. Eng.*, vol. 53, no. 10, pp. 2035–2046, 2006.

[5] S. Hu and L. V. Wang, "Photoacoustic imaging and characterization of the microvasculature," *J. Biomed. Opt.*, vol. 15, no. 1, p. 011101, 2010.

[6] M. Chen, C. Xu, and W. W. Webb, "Endoscope lens with dual fields of view and resolutions for multiphoton imaging," *Opt. Lett.*, vol. 35, no. 16, pp. 2735–2737, 2010.

[7] M. E. Llewellyn, R. P. J. Barretto, S. L. Delp, and M. J. Schnitzer, "Minimally invasive high-speed imaging of sarcomere contractile dynamics in mice and humans," *Nature*, vol. 454, no. 7205, pp. 784–788, 2008.

[8] K. Fujita and N. I. Smith, "Label-free molecular imaging of living cells," *Mol Cells*, vol. 26, no. 6, pp. 530–535, Dec. 2008.

[9] S. V. Plotnikov, A. M. Kenny, S. J. Walsh, B. Zubrowski, C. Joseph, V. L. Scranton, G. A. Kuchel, D. Dauser, M. Xu, C. C. Pilbeam, D. J. Adams, R. P. Dougherty, P. J. Campagnola, and W. A. Mohler, "Measurement of muscle disease by quantitative second-harmonic generation imaging," *J. Biomed. Opt.*, vol. 13, no. 4, p. 044018, 2008.

[10] O. Friedrich, M. Both, C. Weber, S. Schürmann, M. D. H. Teichmann, F. von Wegner, R. H. A. Fink, M. Vogel, J. S. Chamberlain, and C. Garbe, "Microarchitecture is severely compromised but motor protein function is preserved in dystrophic mdx skeletal muscle," *Biophys. J.*, vol. 98, no. 4, pp. 606–616, 2010.

[11] R. Turk, E. Sterrenburg, C. G. C. van der Wees, E. J. de Meijer, R. X. de Menezes, S. Groh, K. P. Campbell, S. Noguchi, G. J. B. van Ommen,

J. T. den Dunnen, and P. A. C. 't Hoen, "Common pathological mechanisms in mouse models for muscular dystrophies," *FASEB J.*, vol. 20, no. 1, pp. 127–129, 2006.

[12] K. A. Lapidos, R. Kakkar, and E. M. McNally, "The dystrophin glycoprotein complex: Signaling strength and integrity for the sarcolemma," *Circ. Res.*, vol. 94, no. 8, pp. 1023–1031, Apr. 2004.

[13] S. I. Head, "Branched fibres in old dystrophic mdx muscle are associated with mechanical weakening of the sarcolemma, abnormal ca2+ transients and a breakdown of ca2+ homeostasis during fatigue," *Exp. Physiol.*, vol. 95, no. 5, pp. 641–656, 2010.

[14] U. Köthe, "Integrated edge and junction detection with the boundary tensor," in *Proc. Int. Conf. Comput. Vis.*, 2003, pp. 424–431.

[15] M. Both, M. Vogel, O. Friedrich, F. von Wegner, T. Künsting, R. H. A. Fink, and D. Uttenweiler, "Second harmonic imaging of intrinsic signals in muscle fibers in situ," *J. Biomed. Opt.*, vol. 9, no. 5, pp. 882–892, 2004.

[16] M. Felsberg and G. Sommer, "The monogenic signal," *IEEE Trans. Image Process.*, vol. 49, no. 12, pp. 3136–3144, Dec. 2001.

[17] U. Köthe, "Low-level feature detection using the boundary tensor," in *Visualization and Processing of Tensor Fields*, J. Weickert and H. Hagen, Eds. Berlin, Germany: Springer, 2006, pp. 63–79.

[18] C. Pastoret and A. Sebille, "Mdx mice show progressive weakness and muscle deterioration with age," *J. Neurol. Sci.*, vol. 129, pp. 97–105, 1995.